

Evaluation of the duty ratio of bacterial flagellar motor by a dynamic load control

Kento Sato¹, Shuichi Nakamura¹, Seishi Kudo¹, and Shoichi Toyabe^{1,*}

¹Department of Applied Physics, Graduate School of Engineering, Tohoku University, Sendai 980-8579, Japan

*Correspondence: toyabe@tohoku.ac.jp

ABSTRACT Bacterial flagellar motor is one of the most complex and sophisticated nano machineries in nature. A duty ratio D is a fraction of time that the stator and the rotor interact and is a fundamental property to characterize the motor but remains to be determined. It is known that the stator units of the motor bind to and dissociate from the motor dynamically to control the motor torque depending on the load on the motor. At low load where the kinetics such as a proton translocation speed limits the rotation rate, the dependency of the rotation rate on the number of stator units N infers D ; the dependency becomes larger for smaller D . Contradicting observations supporting both the small and large D have been reported. A dilemma is that it is difficult to explore a broad range of N at low load because the stator units easily dissociate, and N is limited to one or two at vanishing load. Here, we develop an electrorotation method to dynamically control the load on the flagellar motor of *Salmonella* with a calibrated magnitude of the torque. By instantly reducing the load for keeping N high, we observed that the speed at low load depends on N , implying a small duty ratio. We recovered the torque-speed curves of individual motors and evaluated the duty ratio to be 0.14 ± 0.04 from the correlation between the torque at high load and the rotation rate at low load.

1 INTRODUCTION

Bacterial flagellar motor is a large complex of proteins with a dimension of about 50 nm (1–3). The motor rotates a flagellar filament longer than 5 μm at several hundred Hz unidirectionally and propels the cell body. For a tactic run-and-tumble response, the motor can reverse the rotation with a frequency controlled by an intracellular signal from the sensory protein on the membrane.

The motor implements an automatic torque control. The stator of the bacterial flagellar motor is not static contrary to the name but has a dynamic structure (4) (Fig. 1a). The number of the stator units (N) changes depending on ion motive force (IMF) (5), coupling ion (6), and load (5, 7). For example, when a load on the motor increased, more stator units are incorporated into the motor, and N increases.

The duty ratio D is a fraction of time that the stator and the rotor interact and is a fundamental property to characterize the motor. D is inferred from the dependency of the rotation rate, ω , on N under a low-load condition (Fig. 1b). At high load, ω depends on N independent of D (8–10). This is because the torque generation against load is the rate-limiting step at high load. The motor generates larger torque with more stator units, resulting in a faster rotation. On the other hand, under a low-load condition, the kinetics such as a proton translocation speed limits ω . If D is low, ω is expected to increase with N because of an increased chance of the stator-rotor interaction. If D is high, ω is less affected by N . However, contradicting observations were reported; some experiments implied that ω at vanishing load, referred to a zero-load speed ω_0 below, is independent of N (8, 11, 12) and others implied that ω_0 increases with N (9, 10).

For concluding the dependency, it is necessary to measure ω_0 in a broad range of N at low load. A dilemma is that, the stator units readily dissociate from the motor at low load. In previous experiments, N was limited to one or two.

Here, for evaluating D , we used a calibrated electrorotation method to measure ω_0 of a tethered *Salmonella enterica* serovar Typhimurium cell while keeping N high. This was achieved by quickly reducing the load on the motor by dynamic control of assisting electrorotation torque. If the load changes sufficiently faster than the stator dissociation dynamics, we could measure ω_0 while keeping N high.

We developed the calibration method of the electrorotation established previously (13–16) for applying it to the flagellar motor of the tethered cell. It provides not only the torque magnitude of the electrorotation torque but also the frictional coefficient felt by the motor *in situ* at the same time without any knowledge about the geometry of the probe-motor complex. This implements methodology to recover the precise torque characteristics of individual motors. Before going to the results, we briefly explain the calibration method.

1.1 Calibrated electrorotation method

The electrorotation method imposes an external torque to a microscopic dielectric object by inducing high-frequency alternative current (AC) electric field. The method has been used to apply a dynamically controlled load on the motor of tethered bacterial

cells (17–23) (Fig. 2). However, despite its potential advantages, the method is not widely used mainly due to a lack of the torque calibration method. We previously established the calibration method and successfully applied it to an F₁-ATPase motor and revealed its torque characteristics (13–16). Here, we further develop the method to reduce the experimental noise and apply it to the bacterial flagellar motor.

The electrorotation torque is proportional to the square of the applied voltage amplitude V_0 . Therefore, the load on a motor can be dynamically and continuously controlled by modulating V_0 . Because inertia is negligible in microscopic systems, the torque generated by the motor $T_m(\omega)$ at a rotation rate ω , the viscous torque loaded on the motor, the electrorotation torque, and the thermally fluctuating torque are balanced. The thermal fluctuation is negligible when averaged in a sufficiently long time. Thus, the motor torque becomes

$$T_m(\omega) = \gamma\omega - \alpha V_{\text{sq}}. \quad (1)$$

Here, γ is the rotational frictional coefficient and contains the contributions from the internal friction of the motor and the friction of the cell body and flagellar filament against the fluid. αV_{sq} is an external torque, and V_{sq} is V_0^2 or $-V_0^2$ depending on the sign of the phase shift of the applied AC voltages. The coefficient α depends on multiple factors including the cell shape, the chamber geometry, and the dielectric properties of the cell body and the buffer. Therefore, it is not possible to determine α *a priori*. This has hampered the use of the electrorotation method to measure the motor torque. In the previous papers (18–23), “relative” external torque instead of the exact torque magnitude has been used to plot the torque characteristic.

The calibration is based on the fluctuation-response relation (FRR), which relates the thermal fluctuation to the response to external perturbation under a condition close to the equilibrium (24, 25). Because the motor’s rotation is limited to a low-frequency region and settled at equilibrium at high frequencies, the calibration is possible by comparing the rotational fluctuation and response of rotation against external perturbation at the high frequency. This relation connects the fluctuation $\tilde{C}(f)$ and the response to a small perturbation $\tilde{R}'(f)$:

$$\tilde{C}(f) = 2k_B T \tilde{R}'(f). \quad (2)$$

Here, $\tilde{C}(f)$ is the Fourier transform of the auto-correlation function of the rotational velocity $C(t) = \langle \omega(\tau + t)\omega(\tau) \rangle$ at a frequency f . For an equilibrium Brownian movement, γ is obtained by $\tilde{C}(f) = k_B T / \gamma$. On the other hand, $\tilde{R}'(f)$ is the real part of the frequency response of $\omega(t)$, measured by applying a small sinusoidal torque; $\tilde{R}(f) = w_r e^{i\phi} / N_0$, where f and $N_0 = \alpha V_{\text{sq},0}$ are the frequency and amplitude of the sinusoidal torque. w_r and ϕ are the amplitude and phase of the velocity response. By measuring the fluctuation, $\tilde{C}(f_0)$, and the response, w_r and ϕ , of the rotation rate at sufficiently high frequency f_0 , we can determine α_0 and γ using (2);

$$\alpha = \frac{2w_r \cos \phi}{V_{\text{sq},0}} \gamma, \quad \gamma = \frac{k_B T}{\tilde{C}(f_0)} \quad (3)$$

However, this calibration may be suffered by the interaction between the cell body and the glass surface, which induces a periodic potential on the motor mechanics and yields peaks in the fluctuation spectra. We developed a method to eliminate this effect by using an extended FRR around a local mean velocity developed by Speck and Seifert(26). See the Materials and Methods for details.

2 RESULTS

2.1 Motor torque under low load

The motor of the *Salmonella* cell used here rotates only in the counter-clockwise direction. For exploring the low-load region, we imposed an external torque that assists the rotation in the counter-clockwise direction. A constant assisting torque was applied for 30s and then switched off (Fig. 3a). The magnitude of the torque was roughly tuned so that the load on the motor is close to zero by canceling the viscous load. The equation (1) indicates that such a constant assisting torque shifts the equal-load line (Fig. 1c, bottom).

We observed a steep rise of the rotation speed by the assisting torque and then a stepwise decrease (Fig. 3a). The motor torque T_m calculated by (1) is shown in Fig. 3b. Here, we used averaged values of γ and α in the periods before, during, and after the assist, respectively. The load on the motor was quantified as T_m/ω , which vanished during the assist (Fig. 3b, inset).

During the assist, we observed a stepwise decrease in ω and T_m . After we turned off the assisting torque, the rotation stopped for a while. Then, we observed recovery of the rotation and succeeding stepwise increase in the rotation speed. This recovery phenomenon is supposed to be the so-called resurrection process, in which the stator units bind to the motor (4–8, 27, 28). On the other hand, the stepwise decrease in ω at a vanishing load is thought to be the dissociation of the stator units from the motor. These results suggest that the rotation speed at the vanishing load depends on the number of stator units N (Fig. 1c), implying a small duty ratio. The negative torque observed during the assist is not expected in the large duty ratio (Fig. 1c) and also supports a small duty ratio.

We observed a steep drop of T_m at the beginning of the assist. This is caused mainly by the reduction of the torque generated by each stator unit due to the load change. This is supported by the observation that the step size of the speed during the assist is smaller than that during the resurrection process. We do not deny the possibility that N also decreased instantly at the beginning of the assist.

2.2 Torque-speed curve

For evaluating the value of the duty ratio, we measured the torque-speed (TS) curves of the motors under an assisting torque. We repeated a cycle consisting of a seven-second ramp from $0 V^2$ to $300 V^2$ and three-second intervals alternatively (Fig. 4b and c). The torque was modulated with a 1000-Hz sinusoidal torque with an amplitude of $10 V^2$ for evaluating γ and α *in situ*, with which we can calculate the motor torque by (1).

A typical TS curve is shown in Fig. 4a. The TS curve reached the zero-load state, which is not reachable by a viscous load. In the most experiments, γ was smaller at higher V_{sq} (Fig. 4e). This is because the electric field possibly induces not only a rotational torque but also a dielectric electrophoresis force that pulls the cell apart from the glass surface towards the electrodes. This reduces γ because of the smaller rotation radius and less surface effect (29). The fluctuation patterns of γ and α are similar because γ is multiplied to calculate α (3).

For validating the experimental procedure and the analysis, we applied the method to a stator-less motor. This mutant motor lacks the stator units MotA and MotB and does not generate torque. However, it still has a rotor and flagellar filament and exhibits a rotational Brownian motion. The fluctuation is not free but confined around a certain angular position. The confinement potential is weak, and the motor can be readily rotated under an external torque. We found that the motor torque was zero within the error (Fig. 5a), validating our method. The standard deviations were typically less than 100 pN nm/rad in a broad range of ω , which indicates the accuracy of the method. The deviation was larger for higher external torque. This is because, with higher external torque, T_m is obtained by subtracting a large value of αV_{sq} from a large value of $\gamma\omega$ (1), causing a large statistical error. A small bump was observed around $\omega \approx 50$ Hz. This was caused by the above-described confinement potential specific to the stator-less mutant, and does not affect the torque measurement of the wild-type motors with stator units.

2.3 Evaluation of duty ratio

For evaluating the duty ratio, we compared the TS curves of multiple motors. In Fig. 5b, 76 TS curves of 46 wild-type motors are superposed. We used cells with different expression levels of the stator units for sampling a broad range of N by controlling an Arabinose concentration (Fig. 5c, see Materials and Methods). We observed a broad distribution of the motor torque at high load $T_{m,0}$ calculated by averaging T_m in the first 0.4s of the ramp and a tendency that $T_{m,0}$ becomes smaller with a lower Arabinose concentration. This means that we could sample a broad range of N because $T_{m,0} \propto N$ is expected (8).

The ramp duration of 7 s limits the duration under low load to a few seconds, which is shorter than the dynamics of the stator-unit dissociation (Fig. 3). We expect that the dissociation of the stator units during the ramp is significantly suppressed. However, we still observed a sudden speed change during the ramp for some curves, implying a binding or dissociation of the stator units. For selecting the TS curves, in which N is constant during the ramp, we chose the TS curves with only a slight change in the rotation speed during the ramp. The criterion is that the change in the rotation speed during one second before and after the ramp is less than 1.5 Hz. The TS curves containing a distinct up-and-down change, which is supposedly caused by a series of binding and dissociation of a stator unit, were also excluded from the analysis.

The curve shapes were similar among the TS curves, producing a broad distribution of the zero-load speed ω_0 , supporting a small duty ratio D . For characterizing the TS curves, we divided them into groups according to the value of $T_{m,0}$ (Fig. 5b, inset). Note that we did not specify N in this paper, and therefore there is no one-to-one correspondence between the group and N . We found that ω_0 averaged in each group had significantly distinct values.

We see a clear positive correlation between ω_0 and $T_{m,0}$ (Fig. 6). A simple model neglecting the interactions between the stators (12) predicts a relation

$$\omega_0 = \omega_{0,\max} \left[1 - (1 - D)^N \right]. \quad (4)$$

$\omega_{0,\max}$ is the maximum rotation rate at vanishing load when N is sufficiently large. We evaluated D based on (4) assuming a proportional relation $T_{m,0} = Ns$. The proportional coefficient s corresponds to a torque generated by a single stator at high load. A rough estimation from the resurrection trace (Fig. 3b) gave $s = 130$ pN nm. By fitting (4) with fitting parameters D and $\omega_{0,\max}$, we obtained $D = 0.14 \pm 0.04$ and $\omega_{0,\max} = 306 \pm 54$ Hz. That is, each stator unit interacts with the rotor for a time fraction of 14%. The fitted value of D varies to 0.11 ± 0.03 and 0.16 ± 0.05 for $s = 100$ and 160 pN nm, respectively.

3 DISCUSSION AND CONCLUSION

Contradicting observations have been reported for the dependency of the zero-load speed ω_0 on the number of the stator units N at a vanishing load. Early experiments with the H^+ -motor of *Escherichia coli* implied that ω_0 does not depend on N (8, 11), suggesting a high duty ratio close to one (30, 31). Although they did not assume that N decreases at the zero-load region (5, 7), the independency of ω_0 on N was supported by a recent experiment with *E. coli* motor (12). On the other hand, other group reported that ω_0 of chimeric Na^+ -motor and also H^+ -motor of *E. coli* depends on N (9, 10). A theoretical model based on a small duty ratio of each motor explains this result (32). An experimental challenge regarding this apparent contradiction is that N is limited to one or two under a vanishing load, and it is difficult to observe the N dependency of the rotation rate.

We directly observed a stepwise reduction of the rotation rate at the low-load region, which supposedly corresponds to a change in the stator-unit number N . This is an evidence to support that ω_0 depends on N , suggesting a low duty ratio for the *Salmonella* flagellar motor.

By ramping external torque at a constant rate, we recovered the TS curves of individual motors (Fig. 4). The TS curves reached the zero-load regions, which have been estimated only by extrapolation in the methods using a viscous load such as the beads assay (3, 8, 33–37). We observed that the rotation rate does not converge to a single value in the absence of the load but had a variation (Fig. 5b). The duty ratio was determined to be 0.14 ± 0.04 from the correlation between the motor torque under a high load and ω_0 (Fig. 3). This defines how we model the rotation mechanism of the flagellar motor. A small duty ratio might be effective for a high-speed movement, while a high duty ratio might be effective for a large-torque generation and a long processivity. It would be intriguing to evaluate the duty ratio of the motor of different species living in different environments.

These results were obtained by fully taking the advantage of the electrorotation method for observing the dynamic response to an instant load change. A precise measurement of the TS characteristics and dynamic load control are central to elucidate the torque generation mechanism. A precise shape of the TS curve infers, for example, whether the torque is generated by a power-stroke type or a ratchet type mechanism (38). On the other hand, the measurement of the motor response to a dynamic load modulation would become a powerful tool to investigate the dynamic stator assembly. Beads assay has been used successfully to reveal the motor properties. It is simple and effective to know the average behavior of the motor under each condition. However, the TS curve is blurred by averaging the torque characteristics of multiple motors in the beads assay. Also, the method is not convenient for a dynamical response measurement, whereas there are some attempts to control the load dynamically by changing the viscosity of a buffer (33, 39, 40) or attaching a probe to the flagellum during rotation (7, 12).

A future study specifying N of each TS curve would be helpful to scrutinize the stator dynamics. This may be possible by a combination of fluorescently-labeled stator units and the calibrated electrorotation. Note that the geometry of the tethered cell has an advantage for a total internal reflection fluorescent microscopy because of the short distance between the motor and the bottom glass surface (28). Thus, the methodology demonstrated here would add a new dimension to the study of bacterial flagellar motors.

Finally, we mention that the estimation of γ based on the fluctuation does not require a pre-knowledge about the geometry of the system, and can be applied to broad systems including the beads assay of the bacterial flagellar motor, though precise noise-free fluctuation spectrum is necessary for this. This method should be helpful to provide more reliable values of motor torque and understand the torque-generating mechanism.

This work was supported by JSPS KAKENHI (16H00791 and 18H05427).

4 MATERIALS AND METHODS

4.1 Electrorotation Method

Salmonella strain YSC2123, which lacks *motA*, *motB*, *cheY*, *fimA*, and *fliC* (204–292), was transformed with a plasmid encoding wild-type *motA/motB* (41) (referred to as a wild-type) or not (stator-less mutant).

Cells were grown in L-broth containing 100 $\mu\text{g/ml}$ ampicillin for 5 hours at 30 °C with shaking; 0.0002%, 0.002%, or 0.2% arabinose was added and then incubated for 30 minutes at 30 °C with shaking for protein expression (except the stator-less mutant experiments in Fig. 5a). L-broth was prepared as described previously (42). After replacement of L-broth with the observation buffer (10 mM MOPS(3-Morpholinopropanesulfonic acid) and 10 mM KCl adjusted to pH7.0 with KOH), we partially sheared the sticky flagella filaments by passing the bacterial solution through 25G needle 70 times.

Observation chamber has quadrupolar electrodes with a spacing of 50 μm on the surface of the bottom glass slide. After a 10- μl droplet of the cell solution was placed at the center of the electrodes, a coverslip (Matsunami, Japan) was placed with a thin both-side adhesive tape (10 μm thickness, Teraoka, Japan) as a spacer. Only the top of the both-side adhesive tape was coated by a high-vacuum grease (Shin-Etsu, Japan) so that the top coverslip can be moved. This enables us to move the cells tethered on the top glass slip into the center of the electrodes. After 3 minutes, the solution was replaced with 20 μl of blocking buffer (observation buffer containing 50 mg/ml Perfect Block (MobiTec, Germany)) was flew into the chamber. Perfect block

serves as a blocking agent to suppress the interaction between the cell body and the glass surface. Then, 40 μl of the observation buffer was flew into the chamber to wash free Perfect Block.

We observed the rotation of a tethered cell at a room temperature (24°C) on a phase-contrast upright microscope (Olympus BX51WI, Japan) with a 60 \times objective lens (Olympus, NA=1.42), at 4,000 Hz using a high-speed CMOS camera (Basler, Germany), high-intensity LED (623 nm, 4.8W, Thorlabs, NJ) for illumination, and a laboratory-made capturing software developed on LabVIEW 2014 (National Instruments, TX). The angular position of the cellular body was analysed by an algorithm based on a principal component analysis of the cell image. This method reduces the instrumental noise compared to the centroid-based method.

A 5-MHz sinusoidal voltage with a phase shift of $\pi/2$ was induced on the four electrodes. The signal was generated by a function generator (nf, Japan) controlled by PC and divided by 180° phase distributors (Thamway, Japan). They were amplified by four amplifiers (Analog Devices, MA) and loaded on the electrodes. This generates an electric field rotating at 5 MHz in the center of the electrodes and induces a dipole moment rotating at 5 MHz on the cell body. Since there is a phase delay between the electric field and dipole moment, the cell body is subjected to a constant torque. The magnitude of torque is proportional to the square of the voltages' amplitude V_0 and the volume of the cell body. We modulated V_0 by a signal generated by the multifunction board (National Instruments) equipped on PC. The camera and amplitude signal were synchronized at a time difference less than one microsecond.

4.2 Angular dependency

The periodic perturbation, caused by the interaction between the cell body and the glass surface and also the imperfect voltage balance causes a periodic variation of the rotation rate with the frequencies equal to the integral multiple of the mean rotation rate. These can produce nonequilibrium fluctuation at more than 1,000 Hz and affects the above torque calibration. These nonequilibrium fluctuations are superposed on the equilibrium Brownian spectrum and impede the torque calibration. We suppressed the nonequilibrium fluctuations dramatically by using a modified FRR derived by Speck and Seifert (25, 26); $\tilde{C}_v(f) = 2k_B T \tilde{R}'_v(f)$. Here, $\tilde{C}_v(f)$ and $\tilde{R}'_v(f)$ are the fluctuation and response function of the rotation rate around the local mean velocity defined as $\omega_v(t) \equiv \omega(t) - v(\theta(t))$. $v(\theta_0) = \int_0^T dt \delta(\theta(t) - \theta_0) \omega(t)$ is the local mean velocity at an angular position θ_0 . $\delta(x)$ is the Dirac's delta function. The idea behind this is that the FRR is restored for the rotation around the local mean velocity. The nonequilibrium rotations are embedded in the local mean velocity (25). Therefore, we can estimate γ and α_0 by eliminating the noise by any periodic potential due to, for example, the interaction with the glass surface. Throughout this work, we used $\tilde{C}_v(f)$ and $\tilde{R}'_v(f)$ instead of $\tilde{C}(f)$ and $\tilde{R}'(f)$ in (3) to eliminate the effect of the periodic potential for calculating γ and α_0 .

4.3 Torque-speed curve

The experiments and analysis proceeded as follows. We applied an external torque varied at a constant ramp rate on the tethered cell superposed by a 1000-Hz small sinusoidal torque (Fig. 1b). γ and α had a dependency on the electrorotation strength possibly due to the pulling force towards the electric field. Therefore, we divided the trajectory into windows with a length of 512 frames with 128-frame shifts and calculated γ and α in each window. We averaged $\tilde{C}_v(f)$ in the ranges close to 1,000 Hz: [700 Hz, 900 Hz] and [1100 Hz, 1300 Hz] to obtain γ . α was calculated at 1,000 Hz by a discrete Fourier transform of the rotational trajectory. $\gamma(t)$ and $\alpha(t)$ were smoothed by a linear fitting, and T_m was recovered by (1).

REFERENCES

1. Berg, H. C., 2003. The rotary motor of bacterial flagella. *Annu Rev Biochem.* 72:19–54.
2. Berry, R. M., and J. P. Armitage, 1999. The bacterial flagella motor. *Adv Microb Physiol.* 41:291–337.
3. Sowa, Y., and R. M. Berry, 2008. Bacterial flagellar motor. *Q. Rev. Biophys.* 41:103–132.
4. Block, S. M., and H. C. Berg, 1984. Successive incorporation of force-generating units in the bacterial rotary motor. *Nature* 309:470–2.
5. Tipping, M. J., N. J. Delalez, R. Lim, R. M. Berry, and J. P. Armitage, 2013. Load-Dependent Assembly of the Bacterial Flagellar Motor. *mBio* 4:00551–13.
6. Fukuoka, H., T. Wada, S. Kojima, A. Ishijima, and M. Homma, 2009. Sodium-dependent dynamic assembly of membrane complexes in sodium-driven flagellar motors. *Mol. Microbiol.* 71:825–835.

7. Lele, P. P., B. G. Hosu, and H. C. Berg, 2013. Dynamics of mechanosensing in the bacterial flagellar motor. *PNAS* 110:11839–44.
8. Ryu, W. S., R. M. Berry, and H. C. Berg, 2000. Torque-generating units of the Flagellar motor of *Escherichia coli* have a high duty ratio. *Nature* 403:444.
9. Lo, C.-J., Y. Sowa, T. Pilizota, and R. M. Berry, 2013. Mechanism and kinetics of a sodium-driven bacterial flagellar motor. *PNAS* 110:E2544–E2551.
10. Nord, A. L., Y. Sowa, B. C. Steel, C.-J. Lo, and R. M. Berry, 2017. Speed of the bacterial flagellar motor near zero load depends on the number of stator units. *PNAS* 114:11603–11608.
11. Yuan, J., and H. C. Berg, 2008. Resurrection of the flagellar rotary motor near zero load. *PNAS* 105:1182.
12. Wang, B., R. Zhang, , and J. Yuan, 2017. Limiting (zero-load) speed of the rotary motor of *Escherichia coli* is independent of the number of torque-generating units. *PNAS* 114:12478–12482.
13. Toyabe, S., T. Okamoto, T. Watanabe-Nakayama, H. Taketani, S. Kudo, and E. Muneyuki, 2010. Nonequilibrium energetics of a single F_1 -ATPase molecule. *Phys. Rev. Lett.* 104:198103.
14. Toyabe, S., T. Watanabe-Nakayama, T. Okamoto, S. Kudo, and E. Muneyuki, 2011. Thermodynamic efficiency and mechanochemical coupling of F_1 -ATPase. *Proc. Nat. Acad. Sci. USA* 108:17951–17956.
15. Toyabe, S., and E. Muneyuki, 2013. Experimental thermodynamics of single molecular motor. *Biophys.* 9:91–98.
16. Toyabe, S., and E. Muneyuki, 2015. Single molecule thermodynamics of ATP synthesis by F_1 -ATPase. *New J. Phys.* 17:015008.
17. Iwazawa, J., Y. Imae, , and S. Kobayasi, 1993. Study of the torque of the bacterial flagellar motor using a rotating electric field. *Biophys. J.* 64:925–933.
18. Washizu, M., Y. Kurahashi, H. Iochi, O. Kurosawa, S. Aizawa, S. Kudo, Y. Magariyama, and H. Hotani, 1993. Dielectrophoretic measurement of bacterial motor characteristics. *IEEE Trans. Ind. Appl.* 29:286.
19. Berg, H. C., and L. Turner, 1993. Torque Generated by the Flagellar Motor of *Escherichia coli*. *Biophys. J.* 65:2201–2216.
20. Berry, R. M., L. Turner, and H. C. Berg, 1995. Mechanical limits of bacterial flagellar motors probed by electrorotation. *Biophys. J.* 69:280–286.
21. Berry, R. M., and H. C. Berg, 1996. Torque Generated by the Bacterial Flagellar Motor Close to Stall. *Biophys. J.* 71:3501.
22. Berry, R. M., and H. C. Berg, 1999. Torque Generated by the Flagellar Motor of *Escherichia coli* while Driven Backward. *Biophys. J.* 76:580–587.
23. Sugiyama, S., Y. Magariyama, and S. Kudo, 2004. Forced rotation of Na^+ -driven flagellar motor in a coupling ion-free environment. *BBA* 1656:32.
24. Kubo, R., M. Toda, and N. Hashitsume, 1991. *Statistical Physics II*. Springer, Berlin, second edition.
25. Toyabe, S., and M. Sano, 2015. Nonequilibrium Fluctuations in Biological Strands, Machines, and Cells. *J. Phys. Soc. Jpn.* 84, 102001 (2015). 84:102001.
26. Speck, T., and U. Seifert, 2006. Restoring a fluctuation-dissipation theorem in a nonequilibrium steady state. *EPL* 74:391.
27. Blair, D. F., and H. C. Berg, 1988. Restoration of torque in defective flagellar motors. *Science* 242:1678–81.
28. Leake, M. C., J. H. Chandler, G. H. Wadhams, F. Bai, R. M. Berry, and J. P. Armitage, 2006. Torque-generating units of the Flagellar motor of *Escherichia coli* have a high duty ratio. *Nature* 443:355.
29. Leach, J., H. Mushfique, S. Keen, R. Di Leonardo, G. Ruocco, J. M. Cooper, and M. J. Padgett, 2009. Comparison of Faxén’s correction for a microsphere translating or rotating near a surface. *Phys. Rev. E* 79:026301.

30. Xing, J., F. Bai, R. Berry, , and G. Oster, 2006. Torque–speed relationship of the bacterial flagellar motor. *PNAS* 103:1260–1265.
31. Meacci, G., and Y. Tu, 2009. Dynamics of the bacterial flagellar motor with multiple stators. *PNAS* 106:3746–3751.
32. Nirody, J. A., R. M. Berry, and G. Oster, 2016. The Limiting Speed of the Bacterial Flagellar Motor. *Biophys. J.* 111:557–564.
33. Chen, X., and H. C. Berg, 2000. Torque-Speed Relationship of the Flagellar Rotary Motor of *Escherichia coli*. *Biophys. J.* 78:1036–41.
34. Sowa, Y., H. Hotta, M. Homma, and A. Ishijima, 2003. Torque-speed Relationship of the Na⁺-driven Flagellar Motor of *Vibrio alginolyticus*. *J. Mol. Biol.* 327:1043–51.
35. Che, Y.-S., S. Nakamura, S. Kojima, N. Kami-ike, K. Namba, and T. Minamino, 2008. Suppressor Analysis of the MotB(D33E) Mutation To Probe Bacterial Flagellar Motor Dynamics Coupled with Proton Translocation. *J. Bact.* 190:6660–7.
36. Castillo, D. J., S. Nakamura, Y. V. Morimoto, Y.-S. Che, N. Kami-ike, S. Kudo, T. Minamino, and K. Namba, 2013. The C-terminal periplasmic domain of MotB is responsible for load-dependent control of the number of stators of the bacterial flagellar motors. *biophysics* 9:173–181.
37. Nakamura, S., N. Kami-ike, P. J. Yokota, S. Kudo, T. Minamino, and K. Namba, 2013. Effect of intracellular pH on the torque-speed relationship of bacterial proton-driven flagellar motor. *J. Mol. Biol.* 386:332–338.
38. Nirody, J. A., Y.-R. Sun, and C.-J. Lo, 2017. The biophysicist’s guide to the bacterial flagellar motor. *Adv. Phys. X* 2:324–343.
39. Inoue, Y., C.-J. Lo, H. Fukuoka, H. Takahashi, Y. Sowa, T. Pilizota, G. H. Wadhams, M. Homma, R. M. Berry, and A. Ishijima, 2008. Torque-Speed Relationships of Na⁺-driven Chimeric Flagellar Motors in *Escherichia coli*. *Biophys. J.* 376:1251–1259.
40. Che, Y.-S., S. Nakamura, Y. V. Morimoto, N. Kami-ike, K. Namba, and T. Minamino, 2014. Load-sensitive coupling of proton translocation and torque generation in the bacterial flagellar motor. *Mol. Biol.* 91:175–184.
41. Morimoto, Y. V., Y. S. Che, T. Minamino, and K. Namba, 2010. Proton-conductivity assay of plugged and unplugged MotA/B proton channel by cytoplasmic pHluorin expressed in *Salmonella*. *FEBS Lett.* 584:1268–72.
42. Minamino, T., Y. Imae, F. Oosawa, Y. Kobayashi, and K. Oosawa, 2003. Effect of intracellular pH on rotational speed of bacterial flagellar motors. *J. Bac.* 185:1190–1194.

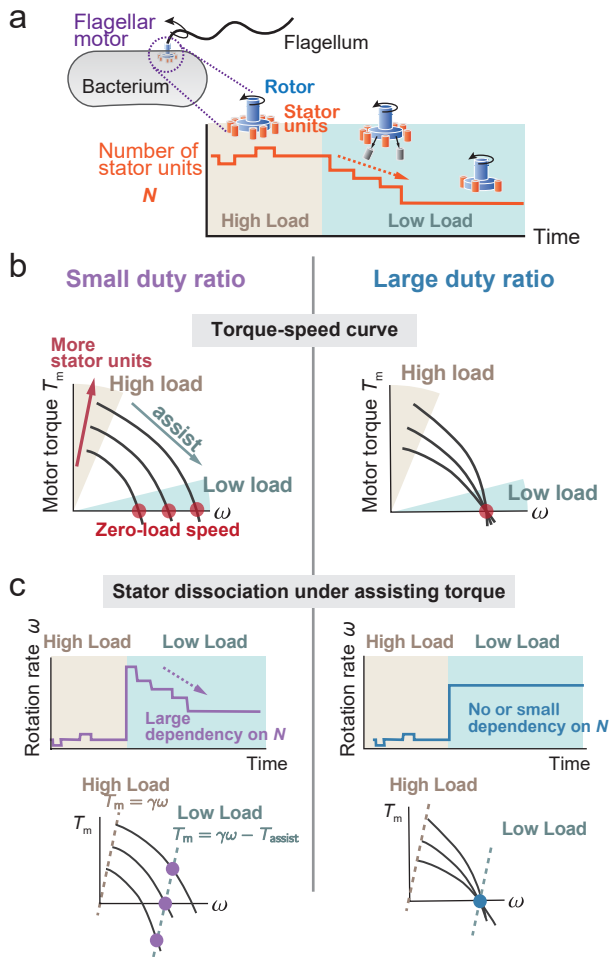


Figure 1: **a**, The stator of the bacterium flagellar motor is a dynamic structure. Its stator units bind to and dissociate from the motor to control the motor torque. The number of stator units N depends on the load on the motor. **b**, At high load, the rotation rate ω as well as the motor torque T_m changes with N . On the other hand, at low load, it is not concluded if they vary with N . We can use this dependency of ω and T_m on N to evaluate the duty ratio. Large dependency implies a small duty ratio, and small dependency implies a large duty ratio. **c**, The duty ratio is also inferred from the reversed-resurrection experiment. As the load on the motor vanishes instantly, N decreases, and then the rotation rate may decrease (small duty ratio) or may keep a similar value (large duty ratio). The motor torque is calculated as $T_m(\omega) = \gamma\omega^2 - T_{\text{assist}}$, where T_{assist} is the external assisting torque by the electrorotation method. Thus, a constant assisting torque by the electrorotation translates the equal-load line parallel.

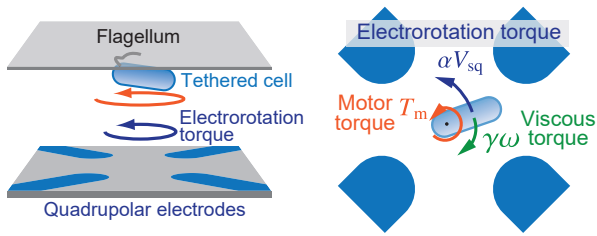


Figure 2: Calibrated electroration method imposes torque with a calibrated magnitude on a tethered cell using high-frequency electric field. The method provides a dynamic torque control to measure the response of the motor, which enables us to measure the torque-speed curves of individual motors.

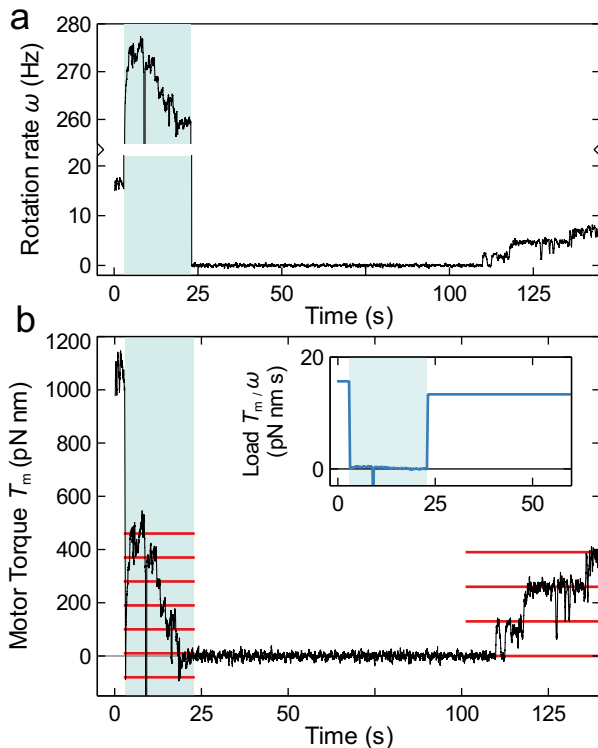


Figure 3: Response of the motor rotation to an assisting torque applied by the calibrated electroration method. **a**, Temporal profile of the rotation rate. The rotation rate increased steeply by an assisting torque (indicated by cyan) and then decreased in a stepwise manner presumably due to the dissociation of the stator units. A steep drop of ω at around 10s might be caused by a nonspecific interaction between the cell body and the glass surface. **b**, Motor torque T_m profile calculated by (1). The horizontal lines are drawn for an eye guide with a spacing of 90 pN nm (left) or 120 pN nm (right). Inset: Load defined as T_m/ω .

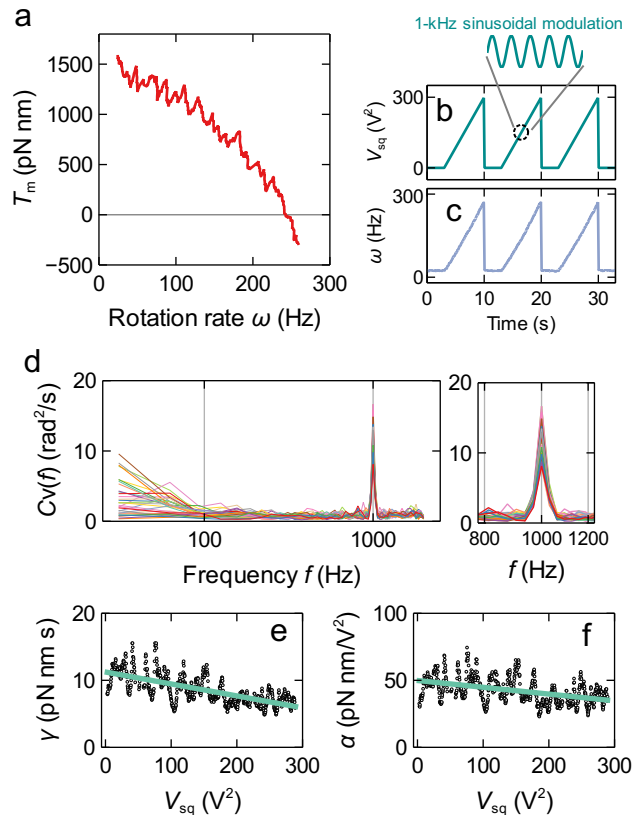
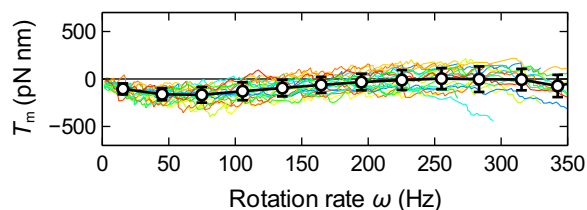
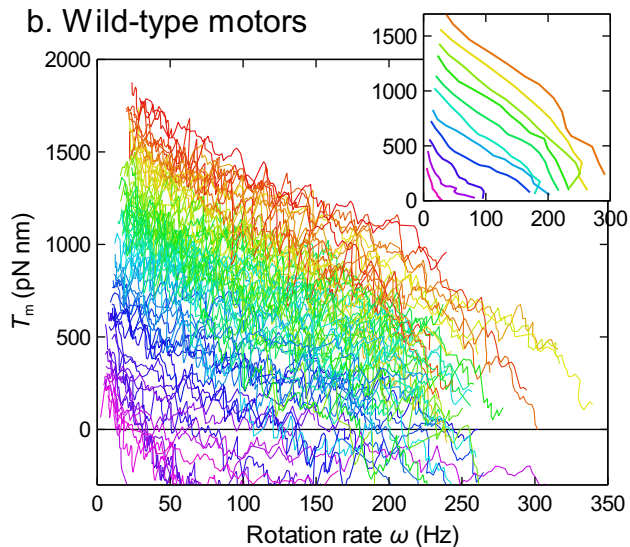


Figure 4: A typical torque-speed curve of a wild-type motor. **a**, The motor torque $T_m(\omega)$ calculated by (1). **b**, Ramp cycles of $V_{sq}(t)$. We repeated a cycle of seven-second ramp from 0 to 300 V² and three-second interval. A ramp in a single cycle is used to recover a TS curve. A 1-kHz sinusoidal perturbation with the amplitude of 10 V² is superposed for the torque calibration. **c**, Rotational rate $\omega(t)$ during cycles. **d**, The power spectra of the rotational rate $C_v(f)$ for 512-frame windows. A steep peak (magnified in the right panel) corresponds to the response to the 1-kHz sinusoidal torque. **e** The frictional coefficient γ calculated from $C_v(f)$ with the 512-frame windows with a 32-frame shift. **f**, The calibration coefficient α . Solid curves in **e** and **f** are linear-fitting curves.

a. Stator-less motors



b. Wild-type motors



c

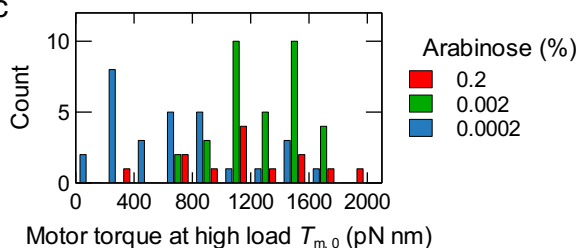


Figure 5: Torque-speed curves. **a**, Torque-speed curves of stator-less (Δ MotA/B) motors. The TS curves of 19 cycles of 8 motors are shown. The black circle is the average in the windows of 30 Hz. The error bars indicate the standard deviation. **b**, 76 TS curves of 46 wild-type motors were superposed. The color indicates the torque at high load. Red color indicates a high torque. Inset: Averaged TS curves in groups divided according to the torque at high load $T_{m,0}$. $T_{m,0}$ is calculated as the average of T_m in the first 0.4s of the ramp. The torque was divided in windows of 120 pN nm. **c**, The histogram of $T_{m,0}$ are plotted separately for different Arabinose concentrations, which control the expression level of the stator units.

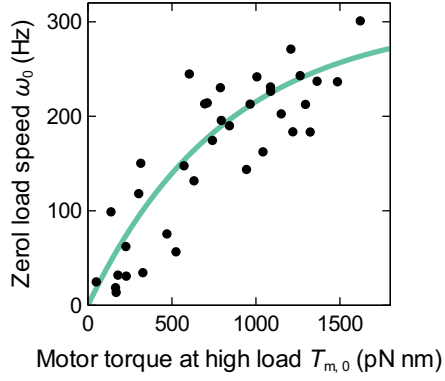


Figure 6: The correlation between the zero-load speed ω_0 and the motor torque at high load $T_{m,0}$. See Fig. 5b for the definition of $T_{m,0}$. A theoretical curve $\omega_0 = \omega_{0,\max} [1 - (1 - D)^{T_{m,0}/s}]$ was fitted (solid curve) with fitting parameters, the maximum speed $\omega_{0,\max}$ and the duty ratio D (12). s is a torque generated by a single stator at high load. We roughly estimated s from the resurrection trace (Fig. 3b). For $s = 130$ pN nm, the fitted values are $\omega_{0,\max} = 306 \pm 54$ Hz and $D = 0.14 \pm 0.04$.